Around the Corner mmWave Imaging in Practical Environments

Laura Dodds
ldodds@mit.edu
MIT

Hailan Shanbhag
hailan.shanbhag@epfl.ch
EPFL

Junfeng Guan
junfeng.guan@epfl.ch
EPFL

Saurabh Gupta
saurabhg@illinois.edu
UIUC

Haitham Hassanieh
haitham.alhassanieh@epfl.ch
EPFL

ABSTRACT

We present the design, implementation, and evaluation of RFlect, a mmWave imaging system capable of producing around-the-corner high-resolution images in practical environments. RFlect leverages signals reflected off complex surfaces (e.g., poles, concave surfaces, or composition of multiple surfaces) to image objects that are not in the RF line-of-sight. RFlect models the reflections and introduces reconstruction algorithms for different types of surfaces. It also leverages a novel method for precisely mapping the location and geometry of the reflecting surface. We also derive the theoretical resolution and coverage for different reflecting surface geometries. We built a prototype of RFlect and performed extensive evaluations to demonstrate its ability to reconstruct the shape of objects around the corner, with an average Chamfer Distance of 2cm and 3D F-Score of 88.6%.

CCS CONCEPTS

• **Networks** → **Sensor networks**.

KEYWORDS

Around-the-Corner Imaging, Millimeter-Wave, mmWave

ACM Reference Format:
Laura Dodds, Hailan Shanbhag, Junfeng Guan, Saurabh Gupta, and Haitham Hassanieh. 2024. Around the Corner mmWave Imaging in Practical Environments. In *The 30th Annual International Conference on Mobile Computing and Networking (ACM MobiCom '24), November 18–22, 2024, Washington D.C., DC, USA.* ACM, New York, NY, USA, 15 pages. https://doi.org/10.1145/3636534.3690671

ACM MobiCom '24, November 18–22, 2024, Washington D.C., DC, USA

ACM ISBN 979-8-4007-0489-5/24/11
https://doi.org/10.1145/3636534.3690671

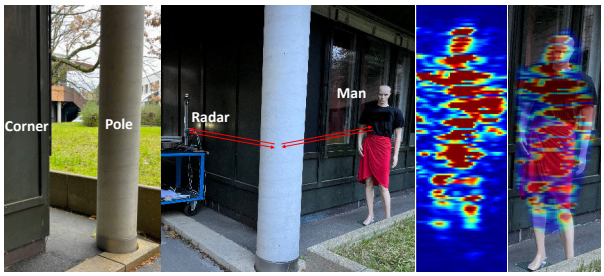

Figure 1: RFlect. is capable to leverage reflections off surrounding surfaces like a pole to produce images of NLOS objects around a corner.

1 INTRODUCTION

In this paper, we explore the problem of non-line-of-sight (NLOS) imaging, specifically producing high-resolution images of objects around the corner. The ability to image objects that are hidden from view around corners and obstacles has several applications. Autonomous vehicles would be able to detect traffic approaching an intersection while hidden behind the corner of a building, allowing them to plan accordingly and avoid collisions. Similarly, an autonomous robot navigating in a factory, warehouse, or restaurant can sense other robots or humans around the corner. In disaster response scenarios, the ability to see around occlusions can allow response teams to efficiently search collapsed buildings and rubble for survivors.

However, NLOS imaging in practical environments is currently not feasible. The majority of conventional imaging modalities, such as cameras and LiDARs, require targets to be in line-of-sight (LOS). One solution is to install a mirror at the corner. However, this requires augmenting the environment at every corner and is therefore not scalable. On the other hand, there has been significant research on using radio-frequency (RF) signals to see through walls [1, 7, 12, 17, 29, 57]. However, RF signals suffer severe attenuation when they traverse through walls and cannot traverse all types of thick walls especially given that they need to pass through two walls two times to get to the object and back, e.g. around the corner of concrete buildings.

More recent work has leveraged the idea of reflecting RF signals off a plane to detect and localize objects around corners [39, 49, 54, 56]. However, simply localizing an object

does not provide any perceptual information on *what* is around the corner. For example, an autonomous vehicle would need to plan differently for a motorcycle than for a bicycle and a search and rescue robot must be able to differentiate between a human and rubble. Although there has been limited work on RF imaging around the corner [22, 44, 46], these works make very strict assumptions about the environment. First, they always assume there is a single, planar surface to reflect the signals off, which is not always the case in practical environments. Additionally, these systems only operate in specially engineered environments where RF-absorptive foam is placed in the area and/or metal is installed on the reflecting wall, limiting their practicality.

In this paper, our goal is to achieve high-resolution mmWave imaging around corners, without making strict assumptions about the environment. In many cases, there is not a single, ideal reflecting plane. Instead, we often need to utilize any available structure or surface to reflect the signals off, such as pillars or poles, concave surfaces, or a combination of different reflectors. These scenarios are challenging for several reasons. First, we need to properly model the reflections on complex surfaces and incorporate them in our processing algorithms to coherently combine the signals received at different antennas in the mmWave radar. For example, using the standard radar processing algorithms in case of multiple reflecting planes would lead to several ghost reflections and bad imaging results. Second, we need to know the precise geometry and location of the complex reflecting surfaces to accurately model the signal reflections. This is because when using mmWave frequencies for imaging, even cm-level errors in modeling the radius of a pole, for example, can lead to severe distortions in the reconstructed image (as we demonstrate in Sec. §9). Finally, we show that convex surfaces such as poles disperse the reflected signals across a much wider angle than the incident beam, resulting in a severe loss of angular resolution, up to 22 times lower compared to a planar reflector in some scenarios.

We present RFlect, which takes the first step towards using wireless signals to image around corners in practical environments. At a high level, 1) RFlect reconstructs NLOS mmWave images by first classifying the dominant reflectors that the signals can reflect off and 2) then estimating their precise geometries and locations using radar data. 3) Then, it uses the reflector model to predict how the signals will reflect and coherently combines the received signals to produce high-resolution images. To enable RFlect, we address the above-mentioned challenges as follows.

• **Mathematical Modeling of NLOS mmWave Imaging:** We derive the mathematical models for mmWave imaging through reflections at complex surfaces such as concave, convex, and multiple planes. We propose algorithms to reconstruct the image in each case by showing how to find the exact reflection point off the surface from each antenna to every voxel in space around the corner and computing the propagation distance of the reflection path in order to coherently combine all received reflections. We also derive the exact theoretical resolution and coverage of mmWave imaging when reflecting off concave and convex surfaces.

• **Precise Reflector Mapping:** We introduce a new technique to precisely map the location and geometry of certain reflecting surfaces, allowing RFlect to avoid severe image degradation due to incorrect reflection path modeling. First, RFlect uses the radar's LOS image to get an initial coarse geometry estimate of the reflecting surface. Unfortunately, for non-planar reflectors, this is not sufficient to get a precise estimate of the reflectors geometry. To address this, RFlect leverages the fact that mmWave radars capture finer resolution information in the phase of the signal which allows us to compute the location and geometry of the reflectors with higher accuracy. However, instead of using a matched filter to construct an image of the surface from which we estimate the geometry, RFlect performs a matched filter over the geometric parameters of the surface e.g. center location and radius in case the reflecting surface is a pole. We describe this method in detail in §7 and show that it significantly improves image quality.

• **Overcoming the Resolution Loss:** As pointed out earlier, convex surfaces result in a massive reduction in resolution. We can compensate for this loss by using a much larger antenna array. However, that would make the array too costly. We observe that the reflected signals from the target only occupy a very small portion of the angular spectrum (e.g., in the direction of the pole). Leveraging this insight, we can use the same number of antennas to build a longer array by increasing the antenna spacing, without suffering from aliasing. This is unlike the case of line-of-sight imaging, which suffers from severe aliasing over the image.

We implemented a prototype of RFlect with a Synthetic Aperture Radar (SAR) based mmWave imaging radar. We extensively evaluate RFlect in various environments and reflecting surfaces (e.g., convex, concave, composite surfaces, etc) to demonstrate its ability to accurately reconstruct the shape of objects in NLOS. In addition to presenting high-resolution radar images, we demonstrate our 3D reconstruction to have an average Chamfer distance of 0.02m and F-Score of 88.6% when compared to a 3D point cloud reconstructed from the Polycam app used on an iPhone 12 Pro. Since 3D reconstruction is difficult to visualize in 2D, we provide an anonymous video link to see the 3D radar point clouds here: https://youtu.be/MqpnturbTIk.

Contributions: The paper has the following contributions:

- RFlect is the first mmWave imaging system capable of producing high-resolution images around the corner in practical environments.
- We introduce a method to precisely map the LOS reflectors and coherently combine signals reflected from complex surfaces to produce high-resolution NLOS images.
- We derive the theoretical impact on resolution and coverage for different geometries of reflecting objects.
- We build a prototype of RFlect, and demonstrate its performance in many real-world environments, with different types of corners and reflecting surfaces.

Limitations: This paper only takes the first steps towards mmWave NLOS imaging in practical environments. We focus on the design of reconstruction algorithms and demonstrate, for the first time, significant results without instrumenting the environment or assuming planar reflectors. However, we acknowledge several limitations of our work that need to be addressed before we can have a fully practical system. For example, RFlect is currently limited to three classes of geometries - convex, concave, and planar - and combinations of multiple such reflectors. Also, our modeling currently assumes specular reflection; future work could investigate how incorporating diffuse scattering, polarization, material properties, etc. can further improve our model. We discuss these limitations, and more, in detail in Sec. §10.

2 RELATED WORK

A. Optical Around-the-Corner: Past work for optical NLOS imaging falls in two main categories: active and passive illumination methods. Active illumination methods use lasers to illuminate the hidden scene [5, 10, 11, 15, 16, 24, 30, 32, 41, 42, 50]. However, these techniques require expensive equipment, such as streak (time-of-flight) cameras along with high-power lasers that can be harmful to humans [42]. More recent work eliminated the need for time-of-flight cameras [5, 16], but makes strict assumptions about objects or the scene such as having highly reflective targets in sparse dark backgrounds. Passive illumination techniques, on the other hand, utilize only ambient lighting [3, 13, 14, 27, 28, 34, 53]. However, many of them can only coarsely detect the presence of moving objects [3] or track objects [27, 28] rather than reconstruct the shapes and images of targets. Those which can reconstruct images of NLOS scenes [13, 14, 34, 53] suffer from low resolution and distortions and have strict setup requirements. For example, [34, 53] require additional occluders in the scene, while [13, 14] rely on speckle correlations to reconstruct the image, so they are applicable only to small objects, as large objects do not cause self-interference. It is worth noting that all aforementioned methods would fail in low visibility (e.g. darkness, smoke, fog, etc.).

RFlect is also related to work which models optical reflections off planar and non-planar surfaces for the purpose of measuring object specularity [25, 26]. We build off these models and adapt them to derive models for around-the-corner mmWave imaging, include unique phenomenon such as reflector-dependent angular resolution and coverage.

B. RF Around-the-Corner: Prior works have explored NLOS sensing using RF signals that bounce off walls or diffract at the edge of corners , including mmWave [9, 35, 36, 39, 45, 48, 49, 51, 54], UWB [18, 19, 37, 43, 56], and terahertz [6, 33] systems. However, these works can only coarsely localize (or image at a very low resolution) the NLOS objects and cannot reconstruct high-resolution images. Mosaic [49] is the only one to consider non-planar reflection surfaces, such as poles, to improve coverage and localization accuracy. We build on top [49] to enable 3D imaging which requires more complex reconstruction algorithms than localization and we derive the theoretical resolution and coverage for convex and concave reflectors.

In the context of NLOS imaging, the closest to our work are [20, 22, 44, 46], which propose reflecting mmWave signals off a singular plane to image NLOS objects. However, these methods have primarily been demonstrated in extremely controlled environments, augmented by RF-absorbing foams and singular planar reflectors made of reflective materials such as metal. RFlect, on the other hand, is able to operate in more practical environments without requiring changes to the environment. It is also worth noting that [46] established a geometric model for around-corner mmWave imaging, but it only considers the simplest scenario with a single planar reflector. Our paper presents for the first time a more generalized mathematical model for complex reflecting surfaces, including concave, convex, and composite surfaces.

C. Other Modalities: Thermal [23] and acoustic [21] imaging have also been studied to reconstruct hidden objects, but have only been demonstrated in well-controlled laboratory settings, with strict requirements on objects.

3 PRIMER ON MMWAVE IMAGING

We start with an overview of RF imaging in LOS (i.e., not reflected) environments. A mmWave radar transmits chirp signals that reflect off objects and are received by the radar and used to measure range. A 2D array of receiver antennas can be used to differentiate reflections along the azimuth and elevation dimensions. Therefore, the received signals can be converted into a 3D radar heatmap, which represents the reflected signal strength of every voxel in 3D space, using various reconstruction algorithms. The most straightforward reconstruction algorithm is to apply matched filters of the reflected signals at baseband. The reflected power $P(v)$ from voxel $v = (x, y, z)$ is:

$$P(v) = \left\| \sum_{i=1}^{A} \sum_{n=1}^{N} s(n,i) e^{j2\pi d(v,i)(f+kn)/c} \right\| \quad (1)$$

where A and N are the # of antennas and samples, $s(n,i)$ is the n^{th} baseband sample of the i^{th} antenna, f and k are the chirp starting frequency and slope , c is the speed of light, $d(v,i)$ is the round-trip distance from the i^{th} antenna to v.

Resolution: The quality of mmWave radar images depends on the range and angular resolutions. While the multi-GHz wide bandwidth of mmWave radars provides cm-level range resolution, (comparable to those of depth cameras and LiDARs), the angular resolution is significantly lower. Angular resolution is inversely proportional to the antenna aperture size and is approximated in azimuth & elevation dimensions:

$$\delta_\theta \approx \frac{\lambda}{D_x \cos(\theta)} \qquad \delta_\phi \approx \frac{\lambda}{D_z \cos(\phi)} \quad (2)$$

where δ_θ (δ_ϕ) is the azimuth (elevation) resolution, D_x (D_z) is the aperture length in the x (z) dimension, and θ (ϕ) is the angle between the voxel and the center of the x (z) aperture. λ is the wavelength of the center frequency.

RF Reflections: When an RF signal reflects off a surface, it will primarily follow one of two types of reflection: scattering (diffuse) or specular reflection. For specular reflection, the angle of incidence is the same as the angle of reflection, while diffuse reflections scatter at unpredictable angles. The type of reflection depends on how smooth the reflecting surface is relative to the signal's wavelength. Since the mm-level wavelength of mmWave radars is relatively long compared to the surface variations of most materials (e.g., concrete, wood, metal, etc.), the majority of reflections are dominated by specular reflections. Since diffuse scattering is difficult to predict and has a smaller contribution to the signal power, we focus on leveraging specular reflections to image around the corner and do not consider diffusion in this paper.

4 SYSTEM OVERVIEW

RFlect is a NLOS mmWave imaging system capable of producing high-resolution images of objects that lie in both RF and visual NLOS. The system can produce images by reflecting signals off LOS reflectors of various geometries, including planar, convex, concave, and composite surfaces. It uses the LOS radar image of the reflecting surfaces to classify their shape and find a rough estimate of their bounds. Then, it refines its estimates to find the exact location and geometry of each reflector in the environment. With this, it predicts how signals reflect off the LOS surfaces and uses this to coherently combine the reflected signals and image objects in NLOS. We describe RFlect's operation in 3 sections:

- **Around-the-Corner Imaging (§5).** First, we develop the mathematical models for imaging in NLOS with reflections from complex surfaces. We describe imaging with planar, convex, concave, and composite surfaces.
- **Theoretical Resolution and Coverage (§6).** Next, since different surfaces will spread or concentrate the signals in space, they change the resolution of the resulting imaging system, as well as the coverage area it can successfully image. We derive the theoretical resolution and coverage area for planar, convex, and concave surfaces.
- **Precise Reflector Mapping (§7).** Finally, RFlect needs to precisely map the LOS reflectors for the imaging models in §5 to be accurate. To achieve high-precision mapping, we leverage the radar data to derive the size and location of every reflector in the environment.

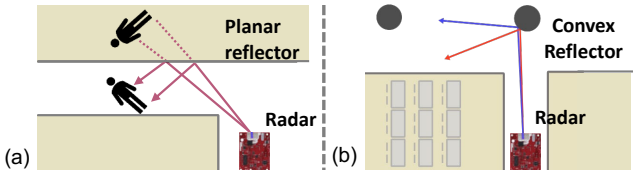

Figure 2: Reflections around the corner of a plane vs. a pole

5 AROUND-THE-CORNER IMAGING

In this section, we will describe how RFlect produces high-resolution images around the corner. For simplicity, in this section, we will assume that the shape and location of all LOS reflectors are known, and we describe how to map these reflectors in §7.

5.1 Planar Surface Imaging

For clarity, we will start by considering a single planar reflector surface. Intuitively, one can think of the reflecting plane like a mirror. The behavior of a planar surface can be seen in Fig. 2(a). Recall from §3 that we can assume that the signals experience primarily specular reflections. This can be seen by the red line, which shows a signal from the radar reflecting specularly towards the object of interest. If we perform ray-tracing without accounting for the reflection, then the angle of arrival and distance will result in the red dashed line ending behind the reflecting wall. This results in a mirrored image of the object located behind the reflecting wall. Leveraging this observation, we can produce an image of the object following two steps: (1) Compute the matched-filter radar image using Eq. 1. The mirrored image will then appear behind the reflecting plane. (2) Reflect the mirrored image over the known plane to produce the final image.

5.2 Convex & Concave Surface Imaging

One might wonder whether we can simply use the same approach for planar surfaces to image over convex and concave surfaces. Unfortunately, this approach will not produce accurate images. For example, Fig. 3(c) shows the result of a real-world experiment measured on a convex surface (a concrete pole) when applying the previous approach, which

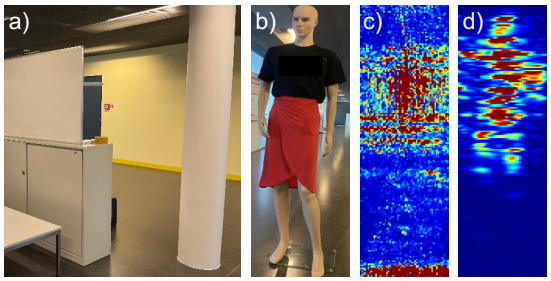

Figure 3: Convex Imaging. Applying standard matched filters results in distorted images while RFlect's method does not.

is significantly distorted. Similar distortions result when applying this method to concave reflectors. This approach fails because the convex and concave surfaces no longer act like a simple planar mirror, but instead spread or concentrate the signal over space as it reflects. For example, Fig. 2(b) shows an example of two signals being reflected off a convex surface, which each travel in different directions depending on which part of the convex surface they reflect off.

We introduce a new method for coherently combining signals reflected off convex/concave surfaces, with 2 steps:

(1) For each voxel-antenna pair, we find the point on the surface p_r that produces a specular reflection between these two points. This is found using the approach in [8].
(2) Next, we perform a matched filter by correlating with the round-trip distance of the specular path (i.e., from antenna to surface to voxel and back along the same path). Formally, this new image $P_c(v)$ can be computed:

$$P_c(v) = \left\| \sum_{i=1}^{A} \sum_{n=1}^{N} s(n,i) e^{j2\pi d(v,p_r,i)(f+kn)/c} \right\| \quad (3)$$

where $d(v, p_r, i)$ is the round-trip distance from the i$^{\text{th}}$ antenna to p_r to voxel v and back along the same path. It can be computed as $d(v, p_r, i) = 2(||v - p_r|| + ||p_r - p_i||)$.

Fig. 3(d) shows the same experiment as above, this time applying our new method for the convex surface. As can be seen, this method is able to successfully reconstruct an image using signals reflected off a convex reflector.

5.3 Multiple Reflecting Surfaces

Finally, in many practical scenarios, there is not one single LOS reflector, but a composition of multiple reflecting surfaces. For example, a cabinet against a wall, an open door and the wall inside of the room, a monitor in front of an office wall, or a pole next to a door could result in multiple sets of reflections. Using reflections from multiple surfaces allows us to reconstruct a more complete image than with a single reflector, as different surfaces have different viewpoints.

If we naively account for only one of the reflecting surfaces, then the reflections from the other surfaces will be incorrectly combined, leading to poor quality and ghost images. We show an example through a real-world experiment with two piecewise planes. The evaluation environment is

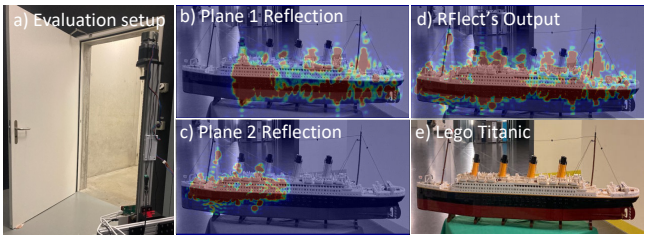

Figure 4: Composite surface imaging. RFlect's output when imaging off of composite surfaces.

shown in Fig. 4(a) and the object, which is a Lego model of the Titanic is shown in Fig. 4(e). If we only account for the plane of the wall, the image will appear as in Fig. 4(b). On the other hand, if we only account for the plane of the door, the image will appear as in Fig. 4(c).

This case is further complicated when reflections bounce off both surfaces in the same path (different surfaces for outgoing & incoming signal). In other words we expect four combinations where the signal travels from the transmitter → Surface 1 *or* Surface 2 → voxel in space → Surface 1 *or* Surface 2 → receiver antenna. This results in seeing three ghost reflections when accounting for one plane. One ghost appears each from paths that reflect off the same surface, and one from the combination of surfaces as shown in Fig. 11.

Instead, RFlect computes the reflections from each antenna to each voxel in space for each of the reflecting surfaces and their combinations by finding the reflection points p_r as described in the previous section. RFlect, then, combines them coherently using a matched filter (Eq. 3). Fig. 4(d) shows the result from the split Lego Titanic and Fig. 11 shows the result for a more complex case. As is evident from the result, our technique is able to successfully reconstruct images coming from multiple reflectors. Furthermore, we reconstruct the entire Lego Titanic, while the reflections from a single reflector was only able to image part of the object, showing how composite surfaces can improve the overall imaging.

6 THEORY: RESOLUTION & COVERAGE

6.1 Resolution

The theoretical resolution of RFlect is dependent not only on the aperture length, but also on the geometry of the reflecting surface. For ease of exposition, we explain how to find the theoretical resolution through Fig. 5. An antenna array can separate any two points spaced further than its LOS resolution (defined in Eq. 2), as shown by the blue lines in Fig. 5. So, how does this separability translate to the non-line-of-sight region? To answer this question, we need to find the angle between two points in our NLOS region that will produce reflections arriving along the blue lines. We do so by reflecting our LOS resolution over our reflecting surface, shown by the red lines. Then, any points along these lines will be separable, and, therefore, our NLOS resolution is the angle between these two vectors.

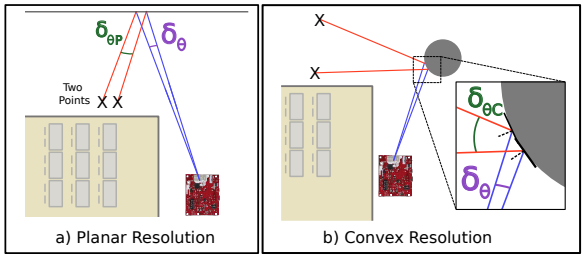

Figure 5: NLOS Imaging Resolution. The NLOS resolution can be found by reflecting the LOS angular resolution over the reflecting surface.

6.1.1 Planar Surfaces. For simplicity, we will derive the horizontal resolution from a planar surface and note that the derivation can easily be extended to the vertical resolution as well. For this reason, we will use 2D coordinates for the remainder of this derivation. Without loss of generality, we assume the radar is located at $(0, 0)$. To find the angular resolution, we start by finding the angle of arrival of the reflected signal from a voxel $v = (x, y)$.

$$x_r = x + |n_x x + n_y y + D| n_x - \frac{n_y(x - p_{r_x}) + n_x(y - p_{r_y})}{1 + \frac{|n_x v_x + n_y v_y + D|}{|n_x p_{r_x} + n_y p_{r_y} + D|}} n_y$$
$$y_r = y + |n_x x + n_y y + D| n_y + \frac{n_y(x - p_{r_x}) + n_x(y - p_{r_y})}{1 + \frac{|n_x v_x + n_y v_y + D|}{|n_x p_{r_x} + n_y p_{r_y} + D|}} n_x \quad (4)$$
$$\theta = \arctan\left(\frac{y_r}{x_r}\right)$$

where (x_r, y_r) is the point on the plane producing a specular reflection from the radar to voxel v, θ is the AoA of the signal from the specular reflection point, and the plane is defined as $n_x x + n_y y + D = 0$ with unit normal $\boldsymbol{n} = (n_x, n_y)$.

Next, we find the resolution, δ_θ, at this AoA using Eq. 2. We know that the aperture's separability at this angle is defined by two rays (r_1 & r_2) centered at θ and spaced by δ_θ.

$$\boldsymbol{r_1} = \begin{bmatrix} \cos(\theta - \frac{\delta_\theta}{2}) \\ \sin(\theta - \frac{\delta_\theta}{2}) \end{bmatrix} \qquad \boldsymbol{r_2} = \begin{bmatrix} \cos(\theta + \frac{\delta_\theta}{2}) \\ \sin(\theta + \frac{\delta_\theta}{2}) \end{bmatrix} \quad (5)$$

We reflect these rays over the plane as described above:

$$\boldsymbol{r_1'} = \boldsymbol{r_1} - 2(\boldsymbol{r_1} \cdot \boldsymbol{n})\boldsymbol{n} \qquad \boldsymbol{r_2'} = \boldsymbol{r_2} - 2(\boldsymbol{r_2} \cdot \boldsymbol{n})\boldsymbol{n} \quad (6)$$

where $\boldsymbol{r_1'}$ and $\boldsymbol{r_2'}$ are the reflections of $\boldsymbol{r_1}$ and $\boldsymbol{r_2}$ over the plane, respectively. Now, the angular resolution, $\delta_{\theta,P}$, is the angle between these two reflected rays:

$$\delta_{\theta,P} = \arccos\left(\frac{\boldsymbol{r_1'} \cdot \boldsymbol{r_2'}}{|\boldsymbol{r_1'}||\boldsymbol{r_2'}|}\right) \quad (7)$$

If we substitute Eqs. 5 and 6 into Eq. 7, we get:

$$\delta_{\theta,P} = \arccos\left(\frac{(\boldsymbol{r_1} - 2(\boldsymbol{r_1} \cdot \boldsymbol{n})\boldsymbol{n}) \cdot (\boldsymbol{r_2} - 2(\boldsymbol{r_2} \cdot \boldsymbol{n})\boldsymbol{n})}{|\boldsymbol{r_1'}||\boldsymbol{r_2'}|}\right) = \arccos\left(\boldsymbol{r_1} \cdot \boldsymbol{r_2}\right)$$
$$\delta_{\theta,P} = \arccos\left(\cos(\theta + \frac{\delta_\theta}{2})\cos(\theta - \frac{\delta_\theta}{2}) + \sin(\theta + \frac{\delta_\theta}{2})\sin(\theta - \frac{\delta_\theta}{2})\right)$$
$$\boxed{\delta_{\theta,P} = \arccos\left(\cos(\delta_\theta)\right) = \delta_\theta} \quad (8)$$

Interestingly, the resolution is equivalent to the LOS resolution (δ_θ). Intuitively, this makes sense as the plane acts like a mirror; it neither spreads nor concentrates the signals.

6.1.2 Convex and Concave Surfaces. Next, we derive the resolution when reflecting over convex or concave surfaces. Since we assume that our convex and concave surfaces are perpendicular to the ground, the horizontal resolution is dependent on the curvature and location of the reflector. In the vertical dimension, however, the surface acts like a simple plane, meaning that the vertical resolution does not change for these surfaces. Therefore, for the remainder of this section, we will only derive the horizontal resolution.

Again, we start by finding the AoA for a voxel $v = (x, y)$.

$$\theta_c = \arctan\left(\frac{y_{r,c}}{x_{r,c}}\right) \quad (9)$$

where $(x_{r,c}, y_{r,c})$ is the specular reflection point between v and the radar. We refer readers to [8] for details on finding this point. θ_c is the AoA of a signal reflected from voxel v over the convex surface. Similar to before, we define two rays centered around the AoA to match the resolution:

$$\boldsymbol{r_{1,c}} = \begin{bmatrix} \cos(\theta_c - \frac{\delta_\theta}{2}) \\ \sin(\theta_c - \frac{\delta_\theta}{2}) \end{bmatrix} \qquad \boldsymbol{r_{2,c}} = \begin{bmatrix} \cos(\theta_c + \frac{\delta_\theta}{2}) \\ \sin(\theta_c + \frac{\delta_\theta}{2}) \end{bmatrix} \quad (10)$$

Next, we find where these rays intersect with the circle.[1]

$$b_1 = -2\boldsymbol{c} \cdot \boldsymbol{r_{1,c}} \qquad b_2 = -2\boldsymbol{c} \cdot \boldsymbol{r_{2,c}}$$
$$d_1 = b_1^2 - 4(||\boldsymbol{c}||^2 - r^2) \qquad d_2 = b_2^2 - 4(||\boldsymbol{c}||^2 - r^2) \quad (11)$$
$$\boldsymbol{p_{i,1}} = \frac{-b_1 \pm \sqrt{d_1}}{2}\boldsymbol{r_{1,c}} \qquad \boldsymbol{p_{i,2}} = \frac{-b_2 \pm \sqrt{d_2}}{2}\boldsymbol{r_{2,c}}$$

where $\boldsymbol{c}$ and r are the center and radius of the circle, and $\boldsymbol{p_{i,1}}$ and $\boldsymbol{p_{i,2}}$ are the points of intersection of $\boldsymbol{r_{1,c}}$ and $\boldsymbol{r_{2,c}}$ with the circle, respectively. The sign in the equation for $\boldsymbol{p_{i,1}}$ depends on the reflecting surface. If it is convex, it is $-$. If it is concave, it is $+$. Then, the normal to the surface of the circle at each of these points can be computed as:

$$\boldsymbol{n_1} = \frac{\boldsymbol{p_{i,1}} - \boldsymbol{c}}{||\boldsymbol{p_{i,1}} - \boldsymbol{c}||} \qquad \boldsymbol{n_2} = \frac{\boldsymbol{p_{i,2}} - \boldsymbol{c}}{||\boldsymbol{p_{i,2}} - \boldsymbol{c}||} \quad (12)$$

where $\boldsymbol{n_1}$ and $\boldsymbol{n_2}$ are the normals to the surface at $\boldsymbol{p_{i,1}}$ and $\boldsymbol{p_{i,2}}$, respectively. With this, we can then compute the direction of the reflected rays:

$$\boldsymbol{r_{1,c}'} = \boldsymbol{r_{1,c}} - 2(\boldsymbol{r_{1,c}} \cdot \boldsymbol{n_1})\boldsymbol{n_1}$$
$$\boldsymbol{r_{2,c}'} = \boldsymbol{r_{2,c}} - 2(\boldsymbol{r_{2,c}} \cdot \boldsymbol{n_2})\boldsymbol{n_2} \quad (13)$$

Finally, the theoretical resolution, $\delta_{\theta,C}$, can be computed as the angle between the two reflected rays:

$$\boxed{\delta_{\theta,C} = \arccos\left(\frac{\boldsymbol{r_{1,c}'} \cdot \boldsymbol{r_{2,c}'}}{|\boldsymbol{r_{1,c}'}||\boldsymbol{r_{2,c}'}|}\right)} \quad (14)$$

[1] We can check if the rays do not intersect if $d_1 < 0$ or $d_2 < 0$.

6.2 Coverage Area

Next, we derive the theoretical coverage for various reflectors. The coverage of our NLOS imaging system is dependent on the size and shape of the reflecting surface.

The coverage area can be found by sweeping the angle of arrival across various angles and reflecting the signals over the LOS surface. Then, the coverage area is any point in space covered by these reflections. In the case of our surfaces (planar, concave, convex), this area is bounded in each dimension by only two rays. In particular, we can obtain the bounds of the coverage area by reflecting a ray over the left-most and right-most bounds of the surface.

6.2.1 Planar Surface. First, we show the coverage of a planar surface. For simplicity, we show the derivation in the horizontal dimension, and note that it can easily be extended to the vertical . We assume the aperture is located at (0,0).

The edge of the coverage area is defined by the reflection over the left and right edge of the plane, computed as:

$$\boldsymbol{r_L} = \boldsymbol{b_L} - 2(\boldsymbol{b_L} \cdot n)n \qquad \boldsymbol{r_R} = \boldsymbol{b_R} - 2(\boldsymbol{b_R} \cdot n)n \tag{15}$$

where $\boldsymbol{r_L}$ and $\boldsymbol{r_R}$ are the rays bounding the coverage area from the left and right , respectively, $\boldsymbol{b_L}$ and $\boldsymbol{b_R}$ are the 2D coordinates of the left and right edge of the plane. Then, the angular coverage, Θ_P, is the angle between these two rays:

$$\boxed{\Theta_P = \arccos\left(\frac{\boldsymbol{r_L} \cdot \boldsymbol{r_R}}{||\boldsymbol{r_L}||||\boldsymbol{r_R}||}\right)} \tag{16}$$

6.2.2 Convex Coverage. Next, we derive the coverage angle for a convex surface. Again, we note that for this surface, the vertical coverage does not change compared to the planar surface, so we only derive the horizontal coverage. For simplicity, we are assuming that the convex reflector is a complete circle, which is often the case(e.g., poles & pillars).

We find the edge of the coverage area by finding the two tangents that intersect the center of the aperture. The slope of the two tangents can be computed as:

$$(x - x_c)^2 + (mx - y_c)^2 = r^2$$

$$m_{1,2} = \frac{-(y_c^2 + 4x_c y_c) \pm \sqrt{(y_c^2 + 4x_c y_c)^2 - 4(x_c^2 + y_c^2 - r^2)(y_c^2 - r^2)}}{2(y_c^2 - r^2)}$$

Next, we find the angle between the two tangents as:

$$\theta_t = \arctan\left|\frac{m_1 - m_2}{1 + m_1 m_2}\right| \tag{17}$$

When a ray is reflected off the circle, it will lie outside of these two tangents. Therefore, the final angular coverage is:

$$\boxed{\Theta_c = 2\pi - \theta_t} \tag{18}$$

6.2.3 Concave Coverage. Finally, we derive the coverage for a concave reflector. Similar to before, we note that the vertical coverage does not change relative to a planar surface, so we derive the horizontal converge. Unlike convex reflectors, we do not assume that concave reflectors are complete circles. For example, curved monitors are only a portion of a circle.

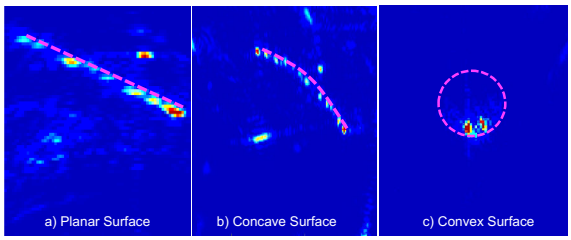

Figure 6: RFlect's Mapping of Different Reflectors. a) Planar surfaces are mapped with the line-of-best fit. b/c) Complex surfaces (e.g., concave / convex) are mapped with our matched-filter algorithm for higher accuracy.

We start by finding the edge of the coverage area as the reflection off the left and right edge of the concave reflector:

$$\boldsymbol{r_{L,c}} = \boldsymbol{b_{L,c}} - 2(\boldsymbol{b_{L,c}} \cdot \boldsymbol{n_R})\boldsymbol{n_L} \qquad \boldsymbol{r_{R,c}} = \boldsymbol{b_{R,c}} - 2(\boldsymbol{b_{R,c}} \cdot \boldsymbol{n_R})\boldsymbol{n_R} \tag{19}$$

Then, the coverage angle, Θ_V, is the angle between them:

$$\boxed{\Theta_V = \arccos\left(\frac{\boldsymbol{r_{L,c}} \cdot \boldsymbol{r_{R,c}}}{||\boldsymbol{r_{L,c}}||||\boldsymbol{r_{R,c}}||}\right)} \tag{20}$$

7 PRECISE REFLECTOR MAPPING

So far, we have described how to image objects using the reflections off complex surfaces. However, until now we have assumed that the exact shape and location of the surfaces were known. Next, we will describe how we map the location and geometry of reflecting surfaces to enable NLOS imaging. The overall process is summarized in Alg. 1.

When mapping reflecting surfaces, it is important to achieve high-accuracy mapping. In fact, we show in §9.4.2 that, for convex surfaces, even a few centimeters of errors can result in significant distortions. To accurately map reflectors, we will use the mmWave radar itself.

We start by computing the bird's eye view (BEV) radar image using a matched filter. We can then identify the LOS surfaces by selecting all pixels above a power threshold τ. For each surface in LOS, we crop the radar image around the LOS surface. If the LOS surface contains a small number of points, this can be classified as a convex surface, since the majority of the surface is reflecting the signal away from the radar. Otherwise, we find the line or arc that best fits the points, as shown in Fig. 6a/b. If the residual error for the line is less than that of the arc, we classify the surface as planar; Otherwise, we classify it as concave. We note that this approach assumes that all surfaces are perpendicular to the ground, which is typically true for most walls and poles. However, it can be easily extended to 3D instead of 2D.

While simply using the line of best fit might be sufficient for planar surfaces, it does not work for more complex surfaces (e.g., convex and concave). Since these reflectors degrade the resolution, they require higher mapping accuracy. Furthermore, due to the specularity of the reflector, the dominant reflection each antenna receives will be its specular

Algorithm 1 RFlect

1) LOS Reflector Classification

$P_{LOS} = \left\|\sum_{i=1}^{A}\sum_{n=1}^{N} s(n,i)e^{j2\pi d(v,i)(f+kn)/c}\right\|$ ▷ Compute LOS SAR image

$s_{LOS} = \{s \in P_{LOS} | s > \tau\}$ ▷ Find LOS surface points (power $> \tau$)

if $|s_{LOS}| < \alpha$ **then**

  $class$ = "Convex" ▷ Convex if low number of points

else if `line_fit_residual`(s_{LOS}) < `arc_fit_residual`(s_{LOS}) **then**

  $class$ = "Planar" ▷ Planar if line of best fit has lower residual

else

  $class$ = "Concave" ▷ Otherwise, concave

end if

2) LOS Reflector Mapping

if $class$ == "Planar" **then**

  $(\hat{x_p}, \hat{y_p}, \hat{n_p})$ = `line_fit`(s_{LOS}) ▷ Use line of best fit

else

  $(\hat{x_c}, \hat{y_c}, \hat{r}) = \max_{(x_c,y_c,r)\in B} S(x_c, y_c, r)$ ▷ Use Eqn. 22

end if

3) NLOS Imaging

if $class$ == "Planar" **then**

  $P(v) = \left\|\sum_{i=1}^{A}\sum_{n=1}^{N} s(n,i)e^{j2\pi d(v,i)(f+kn)/c}\right\|$ ▷ Use Eqn. 1

else

  $P_c(v) = \left\|\sum_{i=1}^{A}\sum_{n=1}^{N} s(n,i)e^{j2\pi d(v,p_r,i)(f+kn)/c}\right\|$ ▷ Use Eqn. 3

end if

reflection off the surface. Since this point is different for every antenna, the reflections will not coherently combine when processed with a normal matched filter, as shown in Fig. 6c.

So, how can we accurately locate these surfaces? At a high level, instead of assuming each antenna is able to receive reflections from every point in space, we instead design a matched filter that accounts for surface specularity. Our algorithm follows three steps:

(1) First, we model the reflector with a small number of parameters. For example, poles are defined by their center point (i.e., a 2D coordinate) and radius.

(2) For a given model, we then find the point on the surface that produces a specular reflection from each antenna back towards itself[8]. Then, we correlate each antenna's received signal with its specular reflection path to produce a score for this model. Formally:

$$S(x_c, y_c, r) = \left\|\sum_{i=1}^{A}\sum_{n=1}^{N} s(n,i)e^{j2\pi d(p_{a,i},p_r)(f+kn)/c}\right\| \quad (21)$$

where $p_{a,i}$ is the i^{th} antenna location, and $S(x_c, y_c, r)$ is the score for a pole centered at (x_c, y_c) with radius r.

(3) We repeat this process, searching over a range of parameters to find the model that best fits the received signals. We bound this search based on the initial object bounds from the LOS radar image. Formally, we select the center and radius that maximizes the score:

$$(\hat{x_c}, \hat{y_c}, \hat{r}) = \max_{(x_c,y_c,r)\in B} S(x_c, y_c, r) \quad (22)$$

where $(\hat{x_c}, \hat{y_c})$, $\hat{r}$ are the final estimated center and radius, and B is the set of possible centers and radii.

Finally, once the LOS reflectors are mapped, we can apply Eqns. 1 and 3 to produce images of the NLOS region.

8 OVERCOMING RESOLUTION LOSS

So far, we have described how we map LOS reflectors and image NLOS objects. Recall from §6 that the theoretical resolution for a convex reflector is drastically reduced compared to that of a planar reflector. In this section, we will discuss how we overcome this resolution loss.

To improve our resolution, we can increase the length of our aperture, which improves our LOS resolution. From Eq. 14, we see that improving our LOS resolution will in turn improve our convex reflected resolution. However, simply increasing the length of our aperture while maintaining the same antenna spacing requires a significantly higher number of antennas, making this approach prohibitively costly for a full array implementation. Typically, increasing the antenna spacing, i.e., subsampling the antenna space, results in severe aliasing for LOS imaging [2].

However, NLOS imaging off a convex reflector does not have the same limitation. Since all signals coming from the NLOS region must reflect off the convex reflector, they will all arrive at the radar within a small portion of the angular spectrum. In fact, this is what causes the loss of resolution in the first place. This allows us to use a much larger antenna spacing before suffering from severe aliasing. In fact, we can increase the aperture from 30cm to 90cm, while using the same total number of antennas, to gain back 87% of our resolution loss without any additional cost.

One additional point is worth noting. While the antenna spacing can be increased for convex reflectors, the same is not true for planar reflectors. Therefore, to successfully operate with different reflector shapes, RFlect could rely on one non-uniform array which is densely-spaced in the middle (for planar reflectors), and sparsely-spaced on the outside (for convex reflectors).

9 EVALUATION

9.1 Implementation & Setup

A. System Implementation: We implemented an end-to-end prototype of RFlect using a TI AWR1843BOOST mmWave radar [40] on a 2D linear stage to produce a synthetic aperture. For planar and convex reflecting surfaces, we use a synthetic aperture of 30×30 cm, while for concave surfaces we extend the aperture to 90×30 cm to compensate for the loss of resolution. Our radar uses a bandwidth of 4GHz, and 512 samples per chirp. We implemented our NLOS imaging models in CUDA to process the 3D radar heatmaps.

B. Evaluation Setup: We evaluated RFlect in various practical

[2]While many works have aimed to overcome this limitation, such as through randomly spacing arrays [55], there is still a limit to the number of antennas that can be used in LOS imaging before aliasing overwhelms the image.

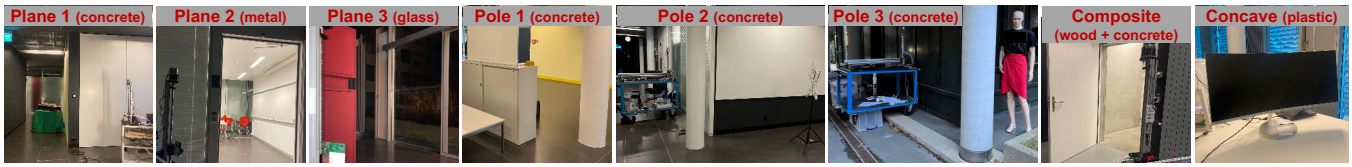

Figure 7: Reflecting Surfaces. RFlect is evaluated on multiple planar, convex, concave and composite surfaces.

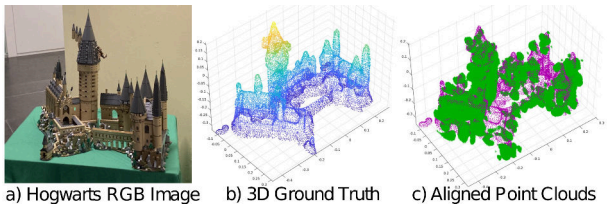

Figure 8: Ground Truth. a) RGB image. b) 3D ground truth scan from iPhone. c) ICP-aligned ground truth (pink) and radar (green) point clouds.

NLOS scenarios, both indoors and outdoors. Figure 7 shows our experiment setup with 3 different planes, 3 different poles, as well as concave surface and composite of multiple planes, which include a variety of reflector materials (concrete, wood, glass, metal, plastic). We tested 8 objects of different shapes, sizes, and materials, shown in Fig. 9.

C. Ground Truth: The ground truth for calculating quantitative metrics is the 3D point cloud reconstruction, shown in Fig. 8, from the Polycam app which uses the LiDAR on iPhone 12 Pro. Each object was imaged with a full 360° scan.

D. Metrics: To evaluate the quality of our NLOS images, we use two quantitative metrics: **Chamfer distance** and **3D F-Score** which are typical metrics for evaluating the quality of 3D point-cloud reconstruction [38, 47]. To compute these metrics, we start by taking all points in our 3D radar image above a certain power threshold to create a 3D point cloud[3]. We then use iterative closest point (ICP)[2] to align the radar point cloud with the ground-truth point cloud as shown in Fig. 8c. Then, we compute the bi-directional Chamfer distance (CD) as the average distance from each point in the radar point cloud to its nearest neighbor in the ground truth point cloud (and vice versa)[47]:

$$CD(P_R, P_G) = \frac{1}{2N_R}\sum_{i=1}^{N_R} d(x_i, P_G) + \frac{1}{2N_G}\sum_{j=1}^{N_G} d(x_j, P_R) \qquad (23)$$

where $CD(P_R, P_G)$ is the chamfer distance between the radar point cloud P_R and the ground truth point cloud P_G (with N_R and N_G points, respectively). $d(x, P)$ is the minimum distance between point x and its nearest neighbor in point cloud P, defined as $d(x, P) = min_{x' \in P}||x - x'||$.

Second, we evaluate the F-Score(FS) based on the precision and recall[38, 52]. Here, precision (recall) is the percent of points within the radar point cloud (ground truth point cloud) whose nearest neighbor in the ground truth point cloud (radar point cloud) are within a threshold τ(0.05m). Formally:

$$PR = \frac{1}{N_R}\sum_{i=1}^{N_R} \mathbb{1}_{d(x_i,P_G)<\tau},\ RE = \frac{1}{N_G}\sum_{j=1}^{N_G} \mathbb{1}_{d(x_j,P_R)<\tau},\ FS = \frac{2\ PR\ RE}{PR + RE}$$

where PR, RE, and FS are the precision, recall, and F-Score, respectively, $\mathbb{1}$ is an indicator variable.

E. Baselines: We compare to two LOS baselines. We place the object directly in front of the radar aperture and apply a standard matched filter algorithm. We repeat this at two distances: *LOS Near* at 1.5 m and *LOS Far* at 4.5 m.

9.2 Qualitative Imaging Results

9.2.1 Imaging off Planar Surfaces. First, we compare the around-the-corner imaging quality of RFlect when using a planar reflector with two LOS baselines(§9.1). To evaluate RFlect, we place the radar roughly 3.5 m from the reflecting wall, and place the target object on the opposite side of the corner roughly 1.5 m from the reflecting wall such that the target object is in NLOS of the radar. The total distance (radar to wall to object) is roughly equivalent to *LOS Far*. For both RFlect and the baselines, we convert the 3D heatmap to 2D by taking the maximum value along the axis of projection.

Fig. 9 shows the 2D heatmaps for *LOS Near* (2nd row), *LOS Far* (3rd row), and RFlect (4th row), and the corresponding RGB images of the target object (1st row). RFlect is able to reconstruct the shape of objects in NLOS settings using planar reflections. For example, the star heatmap clearly shows all 5 arms and the Taj Mahal shows two individual poles and the main tower. Moreover, the performance of RFlect when using planar reflection closely matches the performance of LOS mmWave imaging at the same distance. For example, the Taj Mahal's heatmaps for *LOS Far* and RFlect both show similar resolution. This is expected, since planar reflections do not cause a loss in resolution, as derived in §6.1.

Furthermore, to evaluate RFlect's ability to image in different environments, we capture NLOS images off two different planar reflectors in entirely new environments. Fig. 10(a) shows the results for three different objects overlaid on RGB images of the objects for our second and third plane (1st and second row, respectively). In both cases, RFlect is able to produce accurate heatmaps of the objects, demonstrating RFlect's ability to operate across different environments.

9.2.2 Imaging off Convex Surfaces. Next, we evaluate RFlect's performance when imaging off convex surfaces. In this result,

[3]Since the results depend on the selected power threshold, we evaluate the metrics across a range of thresholds and choose the best performing threshold for each image. This ensures a fair comparison between RFlect and other baseline evaluations.

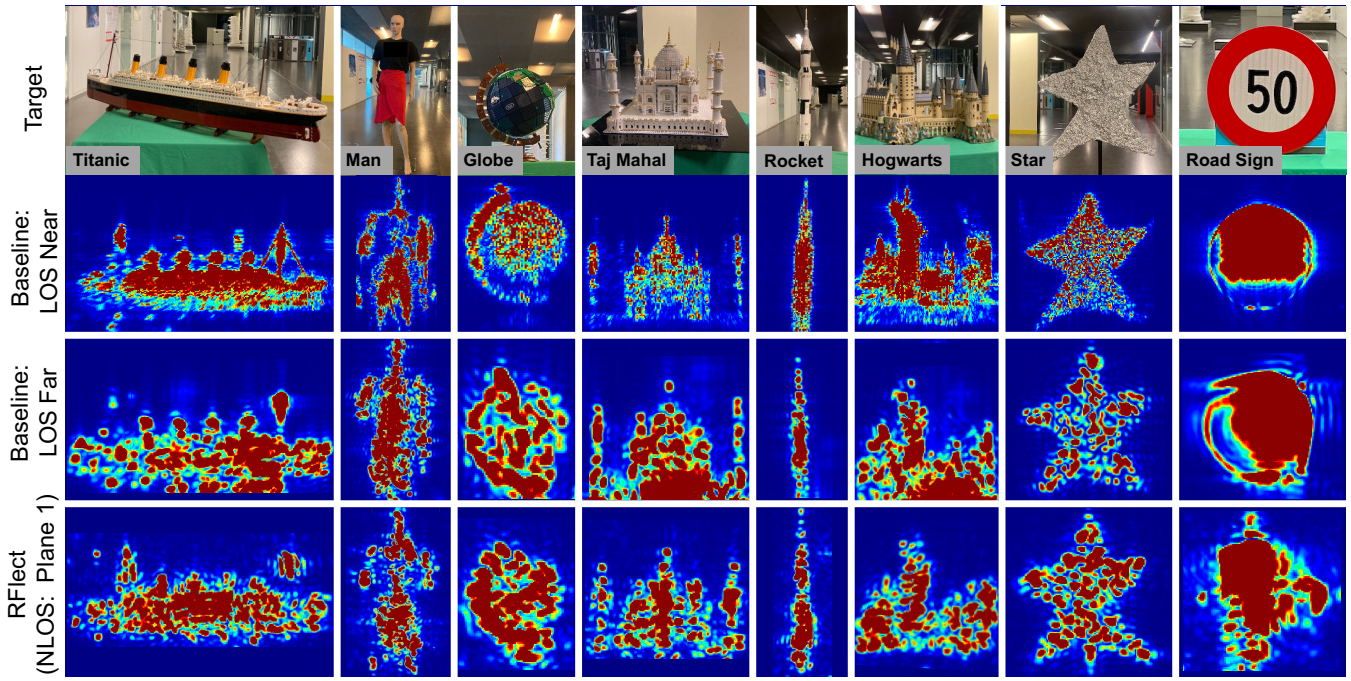

Figure 9: Around Corner Imaging of RFlect compared to baselines. We compare RFlect to baselines of LOS images close to the imaging aperture (1.5m), far from the imaging aperture (4.5m) and images reflected off a wall (planar surface).

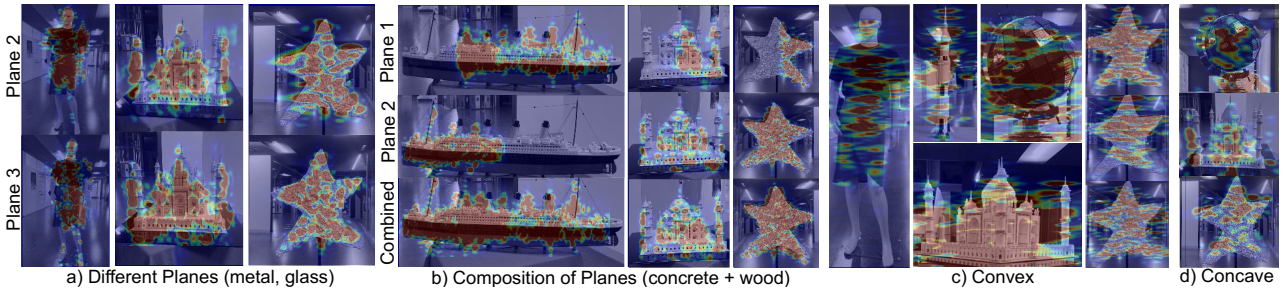

Figure 10: Other reflectors. RFlect's performance on a) different planes shown in Fig. 7, b) composition of planes, c) convex and d) concave reflectors.

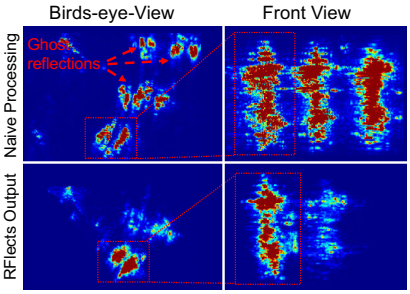

Figure 11: Resolving ghosts. (Top)3 ghosts appear. (Bottom)RFlect separates one mannequin.

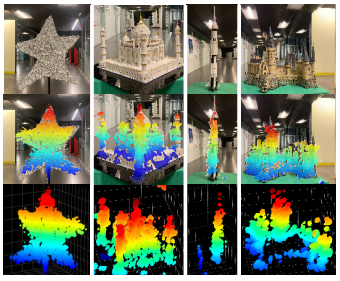

Figure 12: 3D Reconstruction: of star, Taj Mahal, rocket & Hogwarts.

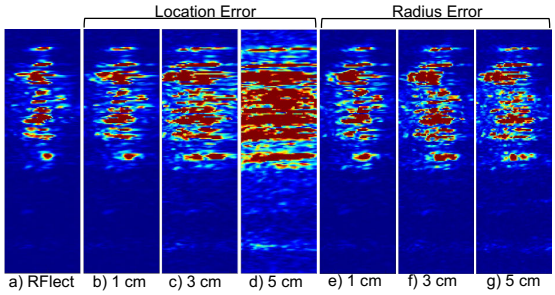

Figure 13: Impact of Mapping Accuracy. Adding errors to location (b, c, d) and radius (e, f, g).

we use poles in a building as the reflecting surface. We place the radar between 1.6m and 2m from the convex surface, and place target objects around the corner at an angle of roughly 90° to the radar (with respect to the surface) and at a distance of 1.5m to 2m from the surface. The radii of our poles are between 0.15m and 0.2m. With this setup, the theoretical resolution derived in §6.1 is between 7° and 10°.

Fig. 10(c) shows the results overlaid on RGB images for 4 different objects on the same pole, as well as results of the star on 3 different poles.

RFlect can produce heatmaps that represent the shape of NLOS objects when reflecting off convex surfaces, showing the value of RFlect's techniques. Moreover, when imaging the same object across three different poles (shown by the 3 star

images on the right), RFlect is able to produce heatmaps of similar quality. This demonstrates RFlect's ability to operate robustly across a variety of different environments (different pole geometries, locations, surrounding environments, etc).

9.2.3 Imaging off Concave Surfaces. Next, we evaluate the performance when imaging off concave surfaces. We place the radar 3 m from a curved monitor with a 1.5m radius (shown in Fig. 7), and placed the target object 3m from the monitor such that the object is completely hidden from the radar. The target object and radar form a roughly 90° angle with respect to the reflecting surface. With this setup, the theoretical resolution is 2°, as derived in §6.1.

Fig. 10(d) shows the results for three different target objects overlaid on RGB images. RFlect is able to produce heatmaps matching the shape of the target object, showing that RFlect's techniques are able to accurately map reflections off concave surfaces for around-the-corner imaging.

9.2.4 Imaging off Multiple Planes. We evaluate RFlect's ability to image around-the-corner when relying on reflections from multiple different surfaces. We place the radar in front of two piecewise planes at a distance of roughly 2m, and place the target object entirely in NLOS roughly 2m from the planes. We plot the 2D thresholded heatmap overlaid on the RGB image of the target object.

Fig. 10(b) shows the resulting image when using only one plane (1st row), using only the second plane (2nd row), and the full image when applying RFlect's methods (3rd row) for three objects. For the Titanic (1st column), imaging with only one plane produces half of the object, while using the other plane produces the other half, due to the limited coverage of each plane. With our composite imaging techniques, RFlect is able to produce an image of the full object by combining reflections off both planes. Similar patterns exist for other objects. This result demonstrates the importance of RFlect's techniques leveraging multiple piecewise reflectors.

Fig. 11 demonstrates the result when an object is imaged off of two planes such that there is a significant overlap in the reflected coverage between the two planes. As described in Sec. §5.3, without using RFlect's method we are left with 3 ghosts. To accurately reconstruct the mannequin, we correlate the signal with each of the possible paths to constructively add all copies at the correct location and eliminate the ghosts. This results with a much stronger reflection coming from the mannequin and places it in the correct location.

9.2.5 3D Reconstruction. So far, we have only shown 2D projections of the heatmap. In fact, RFlect can reconstruct in 3D, which provides much more contextual information. We create a 3D pointcloud with all points in the radar image that are above a certain power threshold. We then color each point in the point cloud based on its z-coordinate. Fig. 12 shows the reference RGB image(1st row), the point cloud overlaid on the image(2nd row), and stand-alone point cloud(3rd row) for some example images produced with planar reflections. However, it is hard to visualize point clouds in 2D. We provide an anonymized video for better visualization which includes additional examples https://youtu.be/MqpnturbTIk.

	LOS Far		Planar	
	CD	FS	CD	FS
Titanic	0.02	0.90	0.03	0.87
Mann.	0.04	0.67	0.04	0.70
Globe	0.01	0.97	0.02	0.96
Taj Mahal	0.03	0.88	0.02	0.90
Rocket	0.01	1.00	0.01	0.99
Hogwarts	0.01	0.97	0.01	0.97
Star	0.01	0.99	0.01	0.99
Road Sign	0.01	0.99	0.04	0.69
	Planar 2		**Planar 3**	
Mann.	0.05	0.70	0.04	0.67
Globe	0.02	0.89	0.02	0.89
Star	0.01	0.99	0.01	0.99

Table 1: LOS Far & Planar. Chamfer distance & F-Scores.

		CD	FS
Convex	**Mann.**	0.06	0.62
	Globe	0.02	0.93
	Taj Mahal	0.03	0.85
	Rocket	0.02	0.94
	Star	0.01	0.99
	Star (P. 2)	0.02	0.99
	Star (P. 3)	0.01	0.94
Concave	**Globe**	0.02	0.95
	Taj Mahal	0.04	0.76
	Star	0.01	0.98
Comp.	**Titanic**	0.03	0.86
	Taj Mahal	0.02	0.92
	Star	0.01	1.0

Table 2: Complex Surfaces. Chamfer distance & F-Scores.

9.3 Quantitative Results

9.3.1 Planar Results. Next, we evaluate the quality of our image using quantitative metrics. We compute the Chamfer distance and F-score (See §9.1) for the Plane 1 images(Fig. 9 4th row), Plane 2 & 3 images (Fig, 10(c)), and *LOS Far* baseline images (Fig. 9 3rd row). Table 1 reports the Chamfer Distance (2nd and 4th columns) and F-Scores (3rd and 5th columns) for *LOS Far* and planar reflections for all objects. We make the following observations:

- For all objects, the Chamfer Distance is 4cm or less, and the F-Score is 69% or higher (with most objects over 87%). This shows that RFlect is able to properly recover the shape of the object when relying on planar reflections.
- Furthermore, for all objects except the road sign, the chamfer distance and F-Score are less than 1cm and 3% different than the results for the same objects in LOS Far, respectively. This demonstrates that RFlect's planar image quality is equivalent to LOS images at the same distance.
- Interestingly, the road sign performs much worse in the planar case than in LOS Far, with an F-Score of 69% (vs 90%). This can be seen visually by the decreased image quality in Fig. 9. This may be due to the high specularity of this object, making it difficult to image when it is not perpendicular to incoming signals.

9.3.2 Convex & Concave Results. We evaluate the quality of our results when using convex and concave surfaces as reflectors. Table 2 shows quantitative results (CD & FS) for convex and concave imaging. We make the following remarks:

- For convex reflectors, RFlect achieves a chamfer distance less than 3cm and an F-score greater than 85% for all objects except the Mannequin. This demonstrates that RFlect is able to successfully leverage convex reflectors to enable high-resolution around-the-corner imaging.

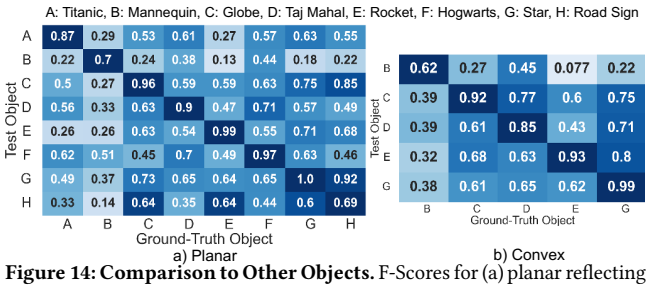

Figure 14: Comparison to Other Objects. F-Scores for (a) planar reflecting surfaces and (b) convex reflecting surfaces compared to ground-truth.

- The mannequin scores the lowest for convex reflections, with a CD of 6cm and an F-score of 62%, likely due to it being our largest object. Furthermore, this is only 2 cm and 8% worse than the mannequin for planar reflections.
- For concave reflectors, RFlect achieves a chamfer distance less than 4cm and an F-score greater than 76% for all objects. This demonstrates RFlect's ability to accurately use concave reflectors to image in NLOS.

Across all results (planar, concave, convex & composite reflections), we report an average Chamfer distance of 2cm and F-Score of 88.6% compared to the ground truth.

9.3.3 Comparison to Other Objects. Finally, we compare the radar point clouds to other object's ground truth point clouds to determine if the radar point clouds are informative enough to identify which object was imaged. We use the same radar point clouds as in §9.2, and compute their F-Score compared to other ground truth point clouds. Fig. 14(a-b) show the confusion matrices when using planar reflections and convex reflections, respectively. The rows denote different test objects (from the radar) and columns are different ground-truth point clouds. The F-Score is written in each grid square, and the grid is colored such that each row is normalized (i.e., the largest value in each row has the darkest blue and the smallest value has the lightest blue). We note that in each row, the highest F-Score occurs when the test object matches the ground-truth (i.e., along the diagonal). This shows that each radar image matches closest with its correct object.

9.4 Microbenchmarks

9.4.1 Impact of Distance. We first evaluate the impact of distance. We image the mannequin in LOS, off a planar surface, and off a convex surface and increase the distance between the radar and the surface (or the object in LOS). Fig. 15 shows the RGB photo and results in a) LOS, b) NLOS using planar reflector and c) NLOS using convex reflector at different distances. The distances listed in the figure are the total distance (from radar to reflecting surface to object). As the distance increases in each case, the image quality degrades slightly. This pattern is most noticeable with the convex reflector, which is expected (See §9.4.3). However, RFlect is still able to image at 7m with planar and 6m with convex reflectors.

9.4.2 Impact of Mapping Accuracy. Next, we evaluate the impact of errors in the convex reflector mapping on the final image. We use the example of the mannequin imaged with reflections off a convex surface from §9.2.2. We add an increasing amount of error (1 cm, 3 cm, 5 cm) to RFlect's estimated location (center y) and radius, independently. Fig. 13a shows RFlect's original output compared to the images when adding small mapping errors in Fig. 13b-g. We note that even with very small errors in the location or radius, the image of the mannequin becomes significantly distorted. This shows the importance of RFlect's surface mapping techniques for producing accurate around-the-corner images.

9.4.3 Theoretical Resolution. Here, we simulate the theoretical angular resolution of RFlect, using our derivations in §6.1, and the radii from our experimental setups (0.175m for convex & 1.5m for concave). First, we simulate the angular resolution vs distance from the radar to the reflecting surface. Fig. 16a plots the results for planar (red), convex (green), and concave (blue). We note that the planar angular resolution is constant vs distance (translating to a linear decrease in cartesian resolution), as expected since planar surfaces do not affect resolution. Convex and concave surfaces see a linear growth in angular resolution with distance[4].

Next, we simulate the resolution vs the angle between the center of the radar aperture and the reflecting surface. Here, negative angles correspond to the left side of the aperture. Fig. 16b plots the results for planar (red), convex (green), and concave (blue) surfaces. We note that for convex and concave surfaces, the resolution reduces from 16° to 6° as the angle ranges from -30° to 40°. Therefore, RFlect has a higher resolution when the pole is on the right side of aperture.

9.5 Long-Range NLOS 2D Mapping

Finally, in Fig. 17, we show how RFlect can produce around-the-corner bird's eye view (BEV) mapping on the horizontal plane, across a much wider area (e.g., multiple buildings). The top row of Fig. 17 illustrates the radar heatmap when using a LOS matched filter algorithm, displaying reflections behind the building walls. The second row shows the ground truth overhead view of the map with thresholded radar points overlaid. The blue points represent LOS reflections and the red points represent the NLOS reflections. By carefully mapping the reflection geometry of each wall, we are able to recreate an accurate 2D BEV map of the streets, which closely matches the ground truth map. This result illustrates that, in addition to 3D imaging of objects, RFlect can also be used for long-distance around-the-corner mapping for applications such as autonomous driving.

10 LIMITATIONS

Although RFlect introduces the first step towards around-the-corner NLOS imaging in practical environments, it has several limitations that require more work to achieve pervasive

[4]Note that concave surfaces can also improve resolution, but only when the target is near the surface, closer than the focal point.

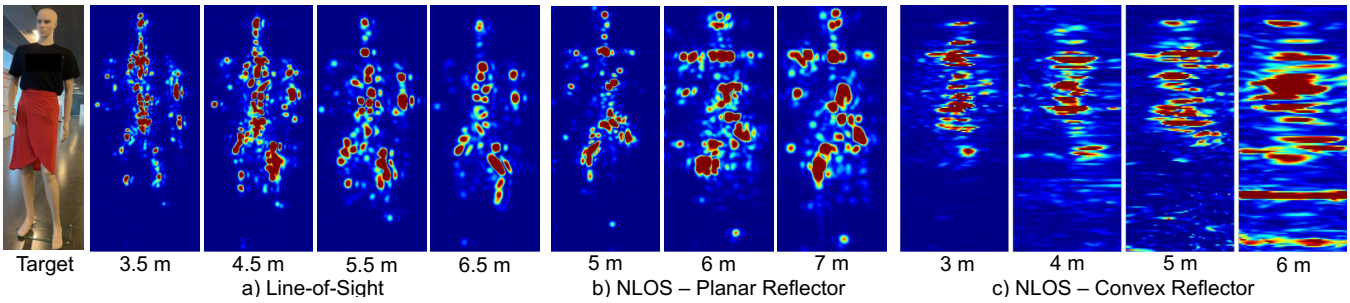

Figure 15: Impact of Distance. The impact of distance when a) in LOS, b) reflecting off planar surfaces, c) reflecting off convex surfaces.

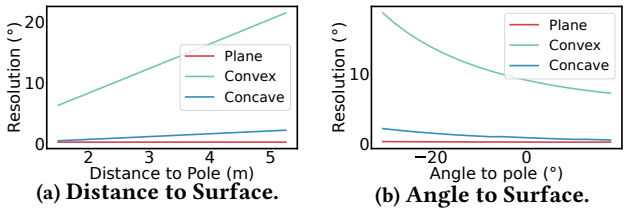

(a) Distance to Surface. **(b) Angle to Surface.**

Figure 16: Theoretical Resolution. Impact of a) distance and b) angle on planar(red), convex(green), and concave(blue) resolution.

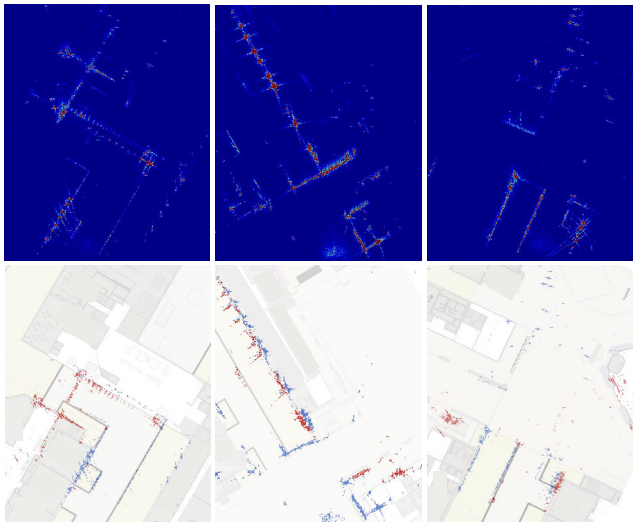

Figure 17: Long-range around-the-corner BEV mapping with surrounding walls: Top: BEV radar heatmap. Bottom: Ground truth map with radar points overlaid. Blue: LOS reflections, red: NLOS reflections.

NLOS imaging:

- For the purpose of this paper, we are assuming three categories of reflectors (concave, convex, and planar) and the combination of multiple such reflectors, which are common in everyday life. While some of our techniques can translate to other low-dimensional surfaces (e.g., spheres, elliptical surfaces, etc), future work is needed to extend RFlect to work with more complex irregular surfaces, for example by constructing 3D representations of the LOS environment to model all the reflections. Despite this, we believe RFlect takes important first steps towards a more generalizable around-the-corner imaging system.
- More generally, RFlect requires the presence of a reflecting surface. While this is the case in many real-world scenarios, RFlect (even with more advanced modeling) would not be able to operate when there are no reflecting surfaces.
- Our techniques assume specular reflections off the LOS scene, with which we achieved accurate imaging across a variety of evaluation environments, as shown in §9. However, while most reflections at mmWave frequencies are specular [31], some very rough surfaces may result in some amount of diffuse scattering, which may decrease the NLOS image quality. It would be interesting for future work to explore the impact of such surfaces and incorporate diffuse scattering into the reflection model. Furthermore, other phenomenon such as polarization, material behaviour, etc. could be further explored to increase the model accuracy.
- Our prototype implementation leverages a synthetic aperture to emulate a 2D array. However, in the future, this can be replaced with a fixed antenna array to eliminate the scanning time, enabling mobile applications such as autonomous vehicles. Alternatively, one could leverage robotic motion (e.g.drones, wheeled robots) to create the synthetic aperture for applications like search and rescue.
- While we empirically demonstrate RFlect's ability to operate across a variety of different scenarios (e.g., reflector material, target material, etc), future work could further expand the theoretical understanding of around-the-corner imaging by analyzing their impact on signal strength. For example, some reflection properties may be identifiable from a LOS radar image to predict the signal strength of the resulting image.

11 CONCLUSION

This paper presented RFlect, the first NLOS imaging system capable of producing high-resolution images in practical environments by leveraging reflections off LOS surfaces. It introduced new techniques for imaging off various surfaces, including convex, concave, and composite surfaces, as well as precisely mapping LOS reflectors to enable accurate image reconstruction. Further, we derived the theoretical resolution & coverage. Our evaluation showed RFlect's ability to successfully reconstruct different objects across various reflectors, both indoor & outdoor.

Acknowledgments We thank the anonymous reviewers and the SENS group (especially Samah Hussein, Jiaming Wang, and Arman Maghsoudnia) for their help and feedback. This research is sponsored by EPFL.

REFERENCES

[1] F. Adib, C.-Y. Hsu, H. Mao, D. Katabi, and F. Durand. Capturing the human figure through a wall. 34(6), nov 2015.

[2] P. J. Besl and N. D. McKay. Method for registration of 3-d shapes. In *Sensor fusion IV: control paradigms and data structures*, volume 1611, pages 586–606. Spie, 1992.

[3] K. L. Bouman, V. Ye, A. B. Yedidia, F. Durand, G. W. Wornell, A. Torralba, and W. T. Freeman. Turning corners into cameras: Principles and methods. In *2017 IEEE International Conference on Computer Vision (ICCV)*, pages 2289–2297, 2017.

[4] I. N. Bronstein, J. Hromkovic, B. Luderer, H.-R. Schwarz, J. Blath, A. Schied, S. Dempe, G. Wanka, and S. Gottwald. *Paperbook of mathematics*, volume 1. Springer-Verlag, 2012.

[5] W. Chen, S. Daneau, C. Brosseau, and F. Heide. Steady-state non-line-of-sight imaging. In *2019 IEEE/CVF Conference on Computer Vision and Pattern Recognition (CVPR)*, pages 6783–6792, Los Alamitos, CA, USA, jun 2019. IEEE Computer Society.

[6] Y. Cui and G. C. Trichopoulos. 3d non-line-of-sight terahertz imaging using mirror folding. In *2022 United States National Committee of URSI National Radio Science Meeting (USNC-URSI NRSM)*, pages 89–90, 2022.

[7] S. Depatla, C. R. Karanam, and Y. Mostofi. Robotic through-wall imaging: Radio-frequency imaging possibilities with unmanned vehicles. *IEEE Antennas and Propagation Magazine*, 59(5):47–60, 2017.

[8] M. Fujimura, P. Hariri, M. Mocanu, and M. Vuorinen. The ptolemy–alhazen problem and spherical mirror reflection. *Computational Methods and Function Theory*, 19:135–155, 2019.

[9] S. Guo, Q. Zhao, G. Cui, S. Li, L. Kong, and X. Yang. Behind corner targets location using small aperture millimeter wave radar in nlos urban environment. *IEEE Journal of Selected Topics in Applied Earth Observations and Remote Sensing*, 13:460–470, 2020.

[10] O. Gupta, T. Willwacher, A. Velten, A. Veeraraghavan, and R. Raskar. Reconstruction of hidden 3d shapes using diffuse reflections. *Optics Express*, 20(17):19096, Aug. 2012.

[11] F. Heide, L. Xiao, W. Heidrich, and M. B. Hullin. Diffuse mirrors: 3d reconstruction from diffuse indirect illumination using inexpensive time-of-flight sensors. In *2014 IEEE Conference on Computer Vision and Pattern Recognition*, pages 3222–3229, 2014.

[12] C. R. Karanam and Y. Mostofi. 3d through-wall imaging with unmanned aerial vehicles using wifi. In *2017 16th ACM/IEEE International Conference on Information Processing in Sensor Networks (IPSN)*, pages 131–142, 2017.

[13] O. Katz, P. Heidmann, M. Fink, and S. Gigan. Non-invasive single-shot imaging through scattering layers and around corners via speckle correlations. *Nature photonics*, 8(10):784–790, 2014.

[14] O. Katz, E. Small, and Y. Silberberg. Looking around corners and through thin turbid layers in real time with scattered incoherent light. *Nature photonics*, 6(8):549–553, 2012.

[15] A. Kirmani, T. Hutchison, J. Davis, and R. Raskar. Looking around the corner using ultrafast transient imaging. *International journal of computer vision*, 95:13–28, 2011.

[16] J. Klein, C. Peters, J. Martín, M. Laurenzis, and M. B. Hullin. Tracking objects outside the line of sight using 2d intensity images. *Scientific reports*, 6(1):32491, 2016.

[17] B. Korany, C. R. Karanam, H. Cai, and Y. Mostofi. Xmodal-id: Using wifi for through-wall person identification from candidate video footage. In *The 25th Annual International Conference on Mobile Computing and Networking*, MobiCom '19, New York, NY, USA, 2019. Association for Computing Machinery.

[18] S. Li, G. Cui, S. Guo, H. Li, L. Kong, and X. Yang. Nlos targets imaging with uwb radar. In *2019 International Conference on Control, Automation and Information Sciences (ICCAIS)*, pages 1–5, 2019.

[19] S. Li, Y. Wang, G. Cui, S. Fan, S. Guo, M. Wang, and X. Yang. Nlos target localization with a uwb radar. In *2019 IEEE Radar Conference (RadarConf)*, pages 1–5, 2019.

[20] Y. Li, Z. Ou, and S. Li. Millimeter-wave non-line-of-sight imaging. In *2022 IEEE 10th Asia-Pacific Conference on Antennas and Propagation (APCAP)*, pages 1–2, 2022.

[21] D. B. Lindell, G. Wetzstein, and V. Koltun. Acoustic non-line-of-sight imaging. In *2019 IEEE/CVF Conference on Computer Vision and Pattern Recognition (CVPR)*, pages 6773–6782, 2019.

[22] X. Liu, S. Wei, J. Wei, J. Shi, X. Zhang, and Y. Li. Non-line-of-sight millimeter-wave radar 3-d sparse reconstruct via msstv method. In *2022 IEEE 9th International Symposium on Microwave, Antenna, Propagation and EMC Technologies for Wireless Communications (MAPE)*, pages 424–427, 2022.

[23] T. Maeda, Y. Wang, R. Raskar, and A. Kadambi. Thermal non-line-of-sight imaging. In *2019 IEEE International Conference on Computational Photography (ICCP)*, pages 1–11, 2019.

[24] C. A. Metzler, F. Heide, P. Rangarajan, M. M. Balaji, A. Viswanath, A. Veeraraghavan, and R. G. Baraniuk. Deep-inverse correlography: towards real-time high-resolution non-line-of-sight imaging. *Optica*, 7(1):63–71, Jan 2020.

[25] A. Morgand, M. Tamaazousti, and A. Bartoli. A multiple-view geometric model of specularities on non-planar shapes with application to dynamic retexturing. *IEEE Transactions on Visualization and Computer Graphics*, 23:2485–2493, 2017.

[26] A. Morgand, M. Tamaazousti, and A. Bartoli. A geometric model for specularity prediction on planar surfaces with multiple light sources. *IEEE Transactions on Visualization and Computer Graphics*, 24(5):1691–1704, 2018.

[27] F. Naser, I. Gilitschenski, A. Amini, C. Liao, G. Rosman, S. Karaman, and D. Rus. Infrastructure-free nlos obstacle detection for autonomous cars. In *2019 IEEE/RSJ International Conference on Intelligent Robots and Systems (IROS)*, pages 250–257. IEEE, 2019.

[28] F. Naser, I. Gilitschenski, G. Rosman, A. Amini, F. Durand, A. Torralba, G. W. Wornell, W. T. Freeman, S. Karaman, and D. Rus. Shadowcam: Real-time detection of moving obstacles behind a corner for autonomous vehicles. In *2018 21st International Conference on Intelligent Transportation Systems (ITSC)*, pages 560–567. IEEE, 2018.

[29] A. Pallaprolu, B. Korany, and Y. Mostofi. Wiffract: A new foundation for rf imaging via edge tracing. In *Proceedings of the 28th Annual International Conference on Mobile Computing And Networking*, MobiCom '22, page 255–267, New York, NY, USA, 2022. Association for Computing Machinery.

[30] R. Ramesh and J. Davis. 5d time-light transport matrix: What can we reason about scene properties? Technical report, 2008.

[31] G. Reina, J. Underwood, G. Brooker, and H. Durrant-Whyte. Radar-based perception for autonomous outdoor vehicles. *Journal of Field Robotics*, 28(6):894–913, 2011.

[32] D. Royo, T. Sultan, A. Muñoz, K. Masumnia-Bisheh, E. Brandt, D. Gutierrez, A. Velten, and J. Marco. Virtual mirrors: Non-line-of-sight imaging beyond the third bounce. *ACM Transactions on Graphics (TOG)*, 42(4):1–15, 2023.

[33] T. Sasaki, E. N. Grossman, and J. R. Leger. Estimation of the 3d spatial location of non-line-of-sight objects using passive thz plenoptic measurements. *Optics Express*, 30(23):41911–41921, 2022.

[34] C. Saunders, J. Murray-Bruce, and V. K. Goyal. Computational periscopy with an ordinary digital camera. *Nature*, 565(7740):472–475, 2019.

[35] N. Scheiner, F. Kraus, F. Wei, B. Phan, F. Mannan, N. Appenrodt, W. Ritter, J. Dickmann, K. Dietmayer, B. Sick, and F. Heide. Seeing around street corners: Non-line-of-sight detection and tracking in-the-wild using doppler radar. In *Proceedings of the IEEE/CVF Conference on*

Computer Vision and Pattern Recognition (CVPR), June 2020.

[36] D. Solomitckii, C. B. Barneto, M. Turunen, M. Allén, G. P. Zhabko, S. V. Zavjalov, S. V. Volvenko, and M. Valkama. Millimeter-wave radar scheme with passive reflector for uncontrolled blind urban intersection. *IEEE Transactions on Vehicular Technology*, 70(8):7335–7346, 2021.

[37] Q. Tang, J. Li, L. Wang, Y. Jia, and G. Cui. Multipath imaging for nlos targets behind an l-shaped corner with single-channel uwb radar. *IEEE Sensors Journal*, 22(2):1531–1540, 2022.

[38] M. Tatarchenko*, S. R. Richter*, R. Ranftl, Z. Li, V. Koltun, and T. Brox. What do single-view 3d reconstruction networks learn? 2019.

[39] K.-P.-H. Thai, O. Rabaste, J. Bosse, D. Poullin, I. Hinostroza, T. Letertre, and T. Chonavel. Around-the-corner radar: Detection and localization of a target in non-line of sight. In *2017 IEEE Radar Conference (RadarConf)*, pages 0842–0847, 2017.

[40] TI Inc. Texas instrument awr1843. https://www.ti.com/product/AWR1843, 2023.

[41] A. Velten, T. Willwacher, O. Gupta, A. Veeraraghavan, M. G. Bawendi, and R. Raskar. Recovering three-dimensional shape around a corner using ultrafast time-of-flight imaging. *Nature communications*, 3(1):745, 2012.

[42] A. Velten, D. Wu, A. Jarabo, B. Masia, C. Barsi, C. Joshi, E. Lawson, M. Bawendi, D. Gutierrez, and R. Raskar. Femto-photography: Capturing and visualizing the propagation of light. *ACM Trans. Graph.*, 32(4), jul 2013.

[43] L. Wang, Q. Tang, Y. Jia, and C. Chen. Multipath imaging for nlos targets behind a t-shaped corridor with single-channel sfcw radar. In *2021 IEEE 6th International Conference on Signal and Image Processing (ICSIP)*, pages 396–400, 2021.

[44] J. Wei, S. Wei, X. Liu, M. Wang, J. Shi, and X. Zhang. Non-line-of-sight imaging by millimeter wave radar. In *2021 IEEE International Geoscience and Remote Sensing Symposium IGARSS*, pages 2983–2986, 2021.

[45] J. Wei, S. Wei, X. Zeng, S. Liu, J. Shi, and X. Zhang. Non-line-of-sight sar imaging by multi-scattering of millimeter-wave. In *2021 CIE International Conference on Radar (Radar)*, pages 259–263, 2021.

[46] S. Wei, J. Wei, X. Liu, M. Wang, S. Liu, F. Fan, X. Zhang, J. Shi, and G. Cui. Nonline-of-sight 3-d imaging using millimeter-wave radar. *IEEE Transactions on Geoscience and Remote Sensing*, 60:1–18, 2022.

[47] F. Williams. Point cloud utils, 2022. https://www.github.com/fwilliams/point-cloud-utils.

[48] T. Woodford, K. Qian, and X. Zhang. Metasight: High-resolution nlos radar with efficient metasurface encoding. In *Proceedings of the 21st ACM Conference on Embedded Networked Sensor Systems*, SenSys '23, page 308–321, New York, NY, USA, 2024. ACM.

[49] T. Woodford, X. Zhang, E. Chai, and K. Sundaresan. Mosaic: Leveraging diverse reflector geometries for omnidirectional around-corner automotive radar. In *MobiSys*, 2022.

[50] S. Xin, S. Nousias, K. N. Kutulakos, A. C. Sankaranarayanan, S. G. Narasimhan, and I. Gkioulekas. A theory of fermat paths for non-line-of-sight shape reconstruction. In *Proceedings of the IEEE/CVF conference on computer vision and pattern recognition*, pages 6800–6809, 2019.

[51] Y. Xu, G. Liu, and T. Jiang. Leveraging rough-relay-surface scattering for non-line-of-sight mmwave radar sensing. *IEEE Internet of Things Journal*, 2023.

[52] Y. Ye, A. Gupta, and S. Tulsiani. What's in your hands? 3d reconstruction of generic objects in hands. 2022.

[53] A. B. Yedidia, M. Baradad, C. Thrampoulidis, W. T. Freeman, and G. W. Wornell. Using unknown occluders to recover hidden scenes. In *Proceedings of the IEEE/CVF Conference on Computer Vision and Pattern Recognition*, pages 12231–12239, 2019.

[54] S. Yue, H. He, P. Cao, K. Zha, M. Koizumi, and D. Katabi. Cornerradar: Rf-based indoor localization around corners. *Proc. ACM Interact. Mob. Wearable Ubiquitous Technol.*, 6(1), mar 2022.

[55] H. Zamani and M. Fakharzadeh. 1.5-d sparse array for millimeter-wave imaging based on compressive sensing techniques. *IEEE Transactions on Antennas and Propagation*, 66(4):2008–2015, 2018.

[56] R. Zetik, M. Eschrich, S. Jovanoska, and R. S. Thoma. Looking behind a corner using multipath-exploiting uwb radar. *IEEE Transactions on Aerospace and Electronic Systems*, 51(3):1916–1926, 2015.

[57] M. Zhao, T. Li, M. A. Alsheikh, Y. Tian, H. Zhao, A. Torralba, and D. Katabi. Through-wall human pose estimation using radio signals. In *2018 IEEE/CVF Conference on Computer Vision and Pattern Recognition*, pages 7356–7365, 2018.

APPENDIX A: CIRCLE REFLECTION POINT

The problem of finding the point on a circle which produces a specular reflection between two given points is known as Alhazen's problem[8]. Here, we briefly describe one known algebraic solution and refer readers to [8] for more details. First, the two given points are modeled as numbers in the complex plane. This solution assumes a unit circle (e.g., centered at 0 with radius 1), so we scale the numbers accordingly:

$$z_1 = \frac{(x_1 - x_c) + (y_1 - y_c)j}{r} \qquad z_2 = \frac{(x_2 - x_c) + (y_2 - y_c)j}{r} \tag{24}$$

where (x_c, y_c) and r are the center and radius of the circle, (x_1, y_1) and (x_2, y_2) are the given points and z_1 and z_2 are their complex numbers, respectively.

Then, the specular reflection point will be one of the four roots of the following polynomial:

$$Au^4 - Bu^3 + Du - E = 0 \tag{25}$$

where $A = \overline{z_1 z_2}$, $B = -(\overline{z_1} + \overline{z_2})$, $D = z_1 + z_2$, and $E = -z_1 z_2$ and where $\bar{\cdot}$ is the conjugate operator. To find the polynomial roots, we can solve the general case of a 4^{th} degree polynomial [4]. We apply a change of variable:

$$\begin{aligned} x = u - \frac{B}{4A}, \quad \alpha &= -\frac{3B^2}{8A^2} + \frac{C}{A} \\ \beta = \frac{B^3}{8A^3}, \qquad \gamma &= -\frac{3B^4}{256A^4} - \frac{BD}{4A^2} + \frac{E}{A} \end{aligned} \tag{26}$$

Then, the new equation is:

$$x^4 + \alpha x^2 + \beta x + \gamma = 0 \tag{27}$$

Next, compute the following intermediate variables:

$$\begin{aligned} P = \frac{\alpha^2}{12} - \gamma, \quad Q &= -\frac{\alpha^3}{108} + \frac{\alpha\gamma}{3} - \frac{\beta^2}{8} \\ w = \sqrt{\alpha + 2y}, \quad U &= -\sqrt[3]{-\frac{Q}{2} + \sqrt{\frac{Q^2}{4} + \frac{P^3}{27}}} \\ z = \frac{\beta}{2w}, \qquad y &= -\frac{5\alpha}{6} + \begin{cases} -\sqrt[3]{Q} & P = 0 \\ U - \frac{P}{3U} & P \neq 0 \end{cases} \end{aligned} \tag{28}$$

Now, the roots of the equation are:

$$u_{1,2,3,4} = \frac{-B}{4A} + \frac{1}{2}\left[sw + r\sqrt{-(\alpha + 2y) - 2\left(\alpha + s\frac{\beta}{w}\right)}\right] \tag{29}$$

where $s, r \in \{-1, 1\}$ are variables to choose the signs, and all 4 combinations create the 4 different roots. Then, we can choose the correct root corresponding to our specular root. For the case of a convex surface, it will be the root that minimizes the round trip distance of the specular path:

$$k = argmin_{i \in \{1,2,3,4\}}(|z_1 - u_i| + |z_2 - u_i|), \quad u_r = u_k \tag{30}$$

Finally, we convert this complex root to our reflection point:

$$p_r = (Re(u_r), Im(u_r)) \tag{31}$$